Boundary Value Problems
a SpringerOpen Journal

RESEARCH Open Access

Non-Newtonian nanofluid flow across an exponentially stretching sheet with viscous dissipation: numerical study using an SCM based on Appell–Changhee polynomials

M.M. Khader[1,2*], M.M. Babatin[1] and Ahmed M. Megahed[2]

*Correspondence:
mmkhader@imamu.edu.sa
[1]Department of Mathematics and Statistics, College of Science, Imam Mohammad Ibn Saud Islamic University (IMSIU), Riyadh, 11566, Saudi Arabia
[2]Department of Mathematics, Faculty of Science, Benha University, Benha, Egypt

Abstract

The objective of this article is to investigate how the properties of a non-Newtonian Williamson nanofluid flow, which occurs due to an exponential stretching sheet placed in a porous medium, are influenced by heat generation, viscous dissipation, and magnetic field. This study focuses on analyzing the heat transfer process by considering the impact of temperature on the thermal conductivity and viscosity of Williamson nanofluids. Additionally, the research significantly contributes by investigating the flow characteristics of these nanofluids when influenced by slip velocity. Using the spectral collocation method (SCM), the equations that describe the current problem are transformed into a collection of ordinary differential equations and then solved. The SCM proposed here basically depends on the properties of the Appell-type Changhee polynomials (ACPs). First, with the aid of ACPs, we give an approximate formula of the derivatives for the approximated functions. Through this procedure, the provided model is transformed into a nonlinear set of algebraic equations. Physical factors of interest, such as skin friction, the Nusselt number, and the Sherwood number, are explained using tabular expressions. Data are displayed as graphs for the nanofluid's velocity, temperature, and concentration. The primary findings showed that increasing the Williamson, magnetic, thermal conductivity, and Brownian parameters significantly improves the thermal field. Finally, testing the suggested method with specific cases from some past literature-based publications reveal a good degree of agreement.

Keywords: Williamson nanofluid; Variable thermal conductivity; Exponential stretching; Slip velocity; Appell–Changhee polynomials; Spectral collocation method; Numerical simulation

1 Introduction

Due to the limited applications of Newtonian fluid models, non-Newtonian fluid research has drawn interest. Non-Newtonian fluids include materials like starch, honey, ketchup, lubricating sprays, and more. Earlier, many non-Newtonian fluid models were proposed. From these a Williamson model was constructed. In 1929, Williamson [1] proposed a non-

Newtonian fluid model that illustrates the rheological characteristics of these fluids. Shear thinning is a characteristic of non-Newtonian fluids like in the Williamson fluid model. In the literature, the Williamson fluid model is the description of a fluid that thins under shear. The Williamson model has been utilized by numerous researchers (see [2–8]) due to its applicability in illuminating fluid dynamics in the preceding decade.

Due to its applicability in the industrial sector, nanotechnology is currently attracting the attention of scientists and researchers, for instance, the application of nanofluids to cool nuclear reactors, regulate heat flow through heat valves, lower automobile radiator temperatures, cool computer processors, etc. Cancer patients are treated in the medical field using medications and radiation delivered by devices made of iron-based nanofluids. By incorporating nanoscale material particles in regular fluids, Choi [9] established the name "nanofluid" and mathematically validated the approach. The nanoparticles mainly consist of metals, nitride ceramics, oxide ceramics, carbide ceramics, and common base fluids like methanol, water, ethylene glycol, and oil. The results of experiments by the authors of [10, 11] proved that nanofluids have a higher thermal conductivity than regular fluids. Mixed convection is a phenomenon where fluid flow involves both natural and forced convection mechanisms simultaneously [12]. It holds significant importance in practical applications, especially in the fields of heat transfer and fluid dynamics. Its significance lies in its capability to affect fluid flow patterns, boost heat transfer rates, enhance energy efficiency, and influence thermal stratification. Precise modeling and analysis of mixed convection phenomena are crucial for optimizing the efficiency and performance of various engineering systems in diverse industries. Due to the significance of mixed convection, Abbas et al. [13] addressed this phenomenon in their study on nanofluid flow in the second grade. After that many authors (see [14–18]) have presented an extensive survey of the flow of nanofluids in various thermo-physical contexts.

In this paper, we will, for the first time, derive an approximate formula of the derivatives with the help of the Appell-type Changhee polynomials and apply it to solve the model under study by using the spectral collocation approaches (see [19, 20]). The most famous advantage of these methods is their capability to generate accurate outcomes with a very small degree of freedom error [21]. They are widely used because of their good properties in the approximation of functions. The orthogonality property of the ACPs is used to approximate functions on their domain. These polynomials have a main and important role in the methods for ODEs [22]. Many researchers used and implemented these polynomials to numerically solve many problems, such as in [23] were they were used to solve the high-dimensional chaotic Lorenz system. Therefore, the primary goal of the current paper is to examine the behavior of a mixed convection boundary layer flow of a non-Newtonian nanofluid flow that includes nanoparticles towards a vertical stretching permeable sheet under slip velocity, nonuniform heat generation, and magnetic field impacts. This goal is motivated by the earlier cited references on the subject of nanofluid models. For the solution of the coupled nonlinear model equations, the spectral collocation method is applied. The motivation of this investigation is to learn more about the non-Newtonian Williamson nanofluid problem and to improve our understanding of it. By examining this research, we hope to add to the body of knowledge, fill in knowledge gaps, and perhaps open the door to breakthroughs in a variety of disciplines, including engineering, materials science, and nanotechnology. The primary objective of this study is to investigate the influence of slip velocity, magnetic field, internal heat generation, and viscous dissipation on the flow behavior of Williamson nanofluid, providing a distinctive viewpoint. The study's novelty and purpose stem from the fact that it is the first of its type to implement the proposed numerical technique to solve the proposed model. The proposed method possesses numerous advantages. The use of Appell–Changhee polynomials in the spectral collocation method results in significant advantages such as exceptional precision, extensive usability, global approximation, efficient execution, high convergence order, and numerical reliability. These advantageous characteristics establish it as a potent and dependable numerical approach suitable for tackling diverse mathematical problems.

This study is organized as follows. A full description of the problem is given in Sect. 2. In Sect. 3, we give some basic concepts about Appell–Changhee polynomials, and an approximation of the D^n via ACPs, with procedure solution using SCM. The code validation is given in Sect. 4. In Sect. 5, we present the results and discussion. Finally, the conclusions are given at the end of the paper through Sect. 6.

2 Basic model

Here, we consider the two-dimensional non-Newtonian Williamson flow of a nanofluid along an exponentially stretched sheet with a constant temperature T_w and concentration C_w. The appropriate values for ambient concentration and temperature are C_∞ and T_∞, respectively. Also, we presume that the constant axial surface temperature T_w is greater than the ambient fluid temperature T_∞. Based on the flow model, the behavior of thermophoresis and Brownian motion are also taken into consideration. Additionally considered are the novel slip velocity, nonuniform heat generation with Brownian motion, and thermophoresis properties. The velocity is assumed to be $U_w = U_0 e^{\frac{x}{L}}$ and the x-axis is taken in the direction of the stretched sheet, where L is a characteristic length and U_0 is a constant velocity (Fig. 1). Furthermore, a suction velocity of v_w is produced by the hypothesis that the sheet is porous.

In addition, the following fluid properties are taken into consideration as a variable besides the assumption of nonuniform heat generation.

(i) Viscosity We assume that the nonlinear exponential function of temperature and the nanofluid viscosity μ are related to one another [24], i.e.,

$$\mu = \mu_\infty e^{-\alpha(\frac{T-T_\infty}{T_w-T_\infty})},$$

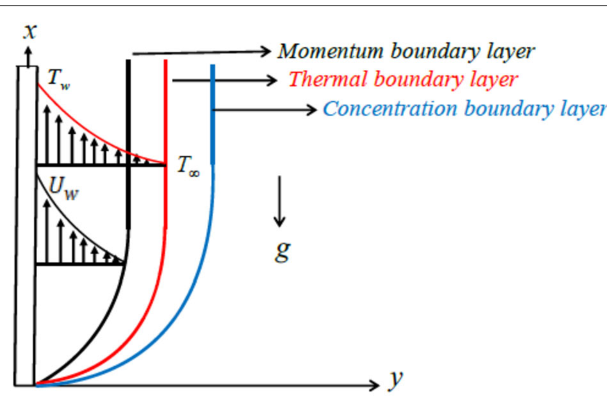

Figure 1 Schematic geometry of the flow problem

where μ_∞ is the nanofluid viscosity away from the sheet and α is the viscosity parameter. Also, this relation explains that the nanofluid viscosity behavior is influenced by the thermal parameter α. Usually, α is regarded as a positive value for a liquid.

(ii) Thermal conductivity Thermal conductivity $\kappa(T)$ demonstrates how a material's conductivity changes. Here, we assume that the relationship between the nanofluid thermal conductivity and the distributed temperature is as follows [24]:

$$\kappa(T) = \kappa_\infty\left(1 + \varepsilon\left(\frac{T - T_\infty}{T_w - T_\infty}\right)\right),$$

where ε is the thermal conductivity parameter, assumed to be small, and κ_∞ is the ambient thermal conductivity. Further, if $\varepsilon = 0$, this relationship indicates that thermal conductivity is a constant.

(iii) Nonuniform heat generation One can observe that the nonuniform heat generation q^* is directly articulated as follows in light of the multiple correlations between nonuniform heat generation and the sheet as well as the ambient temperatures [25]:

$$q^* = \frac{\kappa(T)U_w}{2L\nu_\infty}\left(D_1(T_w - T_\infty)\frac{u}{U_w} + E_1(T - T_\infty)\right),$$

where D_1 is the kinematic viscosity, ν_∞ and E_1 are constants.

The conservative equations after using the boundary layer and Boussinesq estimations yield under the consideration of all the aforementioned factors [26]

$$\frac{\partial u}{\partial x} + \frac{\partial v}{\partial y} = 0, \tag{1}$$

$$\begin{aligned}\rho_\infty\left(v\frac{\partial u}{\partial y} + u\frac{\partial u}{\partial x}\right) &= \frac{\partial}{\partial y}\left(\mu\frac{\partial u}{\partial y} + \mu\frac{\Gamma}{\sqrt{2}}\left(\frac{\partial u}{\partial y}\right)^2\right) - \sigma B_0^2 u - \frac{\mu}{k_0}u \\ &\quad + \rho_\infty g\beta_T(T - T_\infty) + \rho_\infty g\beta_c(C - C_\infty),\end{aligned} \tag{2}$$

$$\begin{aligned}\rho_\infty c_p\left(u\frac{\partial T}{\partial x} + v\frac{\partial T}{\partial y}\right) &= \frac{\partial}{\partial y}\left(k(T)\frac{\partial T}{\partial y}\right) + \rho_\infty c_p\tau\left[D_B\frac{\partial C}{\partial y}\frac{\partial T}{\partial y} + \frac{D_T}{T_\infty}\left(\frac{\partial \mathrm{T}}{\partial y}\right)^2\right] \\ &\quad + \mu\left(\left(\frac{\partial u}{\partial y}\right)^2 + \frac{\Gamma}{\sqrt{2}}\left(\frac{\partial u}{\partial y}\right)^3\right) + \sigma B_0^2 u^2 + q^*,\end{aligned} \tag{3}$$

$$u\frac{\partial C}{\partial x} + v\frac{\partial C}{\partial y} = \frac{D_T}{T_\infty}\frac{\partial^2 T}{\partial y^2} + D_B\frac{\partial^2 C}{\partial y^2}, \tag{4}$$

and the related boundary conditions are [8]:

$$\begin{aligned}&u = U_w + \frac{\lambda_1}{\mu_\infty}\left(\mu\frac{\partial u}{\partial y} + \mu\frac{\Gamma}{\sqrt{2}}\left(\frac{\partial u}{\partial y}\right)^2\right), \qquad v = -v_w = -V_0 e^{\frac{x}{2L}}, \\ &T = T_w, \qquad C = C_w, \quad \text{at } y = 0,\end{aligned} \tag{5}$$

$$u \to 0, \qquad T \to T_\infty, \qquad C \to C_\infty, \quad \text{as } y \to \infty. \tag{6}$$

It is crucial to note that the momentum equation (2) introduces two significant additions: the inclusion of a variable thermal viscosity and the mixed convection term. Similarly, the energy equation (3) incorporates the viscous dissipation term and the internal heat generation term. Also, it is important to emphasize that the initial component of equation (5) represents the phenomenon of slip velocity, where the x- and y-axis coefficients of the fluid velocity vectors are u and v, respectively; D_B, Γ, B_0 represent diffusivity of the Brownian motion, the Williamson parameter, and the magnetic field intensity; τ is the ratio of the nanoparticle's effective heat capacitance to that of the base fluid, V_0 is the constant suction velocity, k_0 is the porous medium's permeability, D_T is the thermophoretic diffusion coefficient, σ is electrical conductivity, β_c is the coefficient of concentration expansion, β_T is the temperature expansion factor, g is the acceleration due to gravity, c_p is the specific heat at constant pressure, λ_1 is the factor of slip velocity, and ρ_∞ is the ambient density.

Now, the following dimensionless transformation is used to convert the nonlinear partial differential equations (1)–(4) into nonlinear ordinary differential equations (ODEs), assuming the apposite similarity variable $\eta = y\sqrt{\frac{U_0\rho_\infty}{2L\mu_\infty}}e^{\frac{x}{2L}}$ as shown below [26]:

$$u = U_0 e^{\frac{x}{L}} f'(\eta), \qquad v = -\sqrt{\frac{U_0\mu_\infty}{2L\rho_\infty}}e^{\frac{x}{2L}}\bigl(f(\eta) + \eta f'\bigr), \tag{7}$$

$$T = T_\infty + (T_w - T_\infty)\theta(\eta), \qquad C = C_\infty + (C_w - C_\infty)\phi(\eta), \tag{8}$$

where f is the dimensionless stream function, $\theta(\eta)$ is the dimensionless temperature, and $\phi(\eta)$ is the dimensionless concentration. Now, equation (7) enables the continuity equation (1) to be satisfied precisely. The following dimensionless system of ODEs with associated boundary constraints is obtained from the system (2)–(4) with boundary constraints (5)–(6) by invoking transformation (7)–(8). So, we have

$$\begin{aligned}&\left(\bigl(1 + W_e f''\bigr)f''' - \alpha\theta' f''\left(1 + \frac{W_e}{2}f''\right)\right)e^{-\alpha\theta}\\&\qquad + ff'' - 2f'^2 - Mf' - \gamma e^{-\alpha\theta}f' + \mathrm{Gr}_T\theta + \mathrm{Gr}_C\phi = 0,\end{aligned} \tag{9}$$

$$\begin{aligned}&\frac{1}{\mathrm{Pr}}\bigl((1 + \varepsilon\theta)\theta'' + \varepsilon\theta'^2\bigr) + f\theta' - f'\theta + \mathrm{Nt}\bigl(\theta'\bigr)^2 + \mathrm{Nb}\theta'\phi' + M\mathrm{Ec}f'^2\\&\qquad + \mathrm{Ec}\left(f''^2 + \frac{W_e}{2}f''^3\right)e^{-\alpha\theta} + \left(\frac{1 + \varepsilon\theta}{\mathrm{Pr}}\right)\bigl(D_1 f' + E_1\theta\bigr) = 0,\end{aligned} \tag{10}$$

$$\phi'' + \mathrm{Sc}f\phi' + \frac{\mathrm{Nt}}{\mathrm{Nb}}\theta'' = 0, \tag{11}$$

subject to the following restrictions on boundaries:

$$f'(0) = 1 + \lambda\left(f'' + \frac{W_e}{2}f''^2\right)e^{-\alpha\theta(0)}, \qquad f(0) = S, \qquad \theta(0) = 1, \qquad \phi(0) = 1, \tag{12}$$

$$f'(\infty) \to 0, \qquad \theta(\infty) \to 0, \qquad \phi(\infty) \to 0, \tag{13}$$

where $M = \frac{\sigma B_0}{\rho_\infty U_0}e^{\frac{-x}{L}}$ is the magnetic parameter, $\lambda = \lambda_1\sqrt{\frac{U_w}{2L\nu_\infty}}$ is the slip velocity parameter, $S = V_0\sqrt{\frac{2L}{U_0\nu_\infty}}$ is the suction parameter, $W_e = (\frac{U_0}{2})^{\frac{2}{3}}\frac{\Gamma}{\sqrt{L}}e^{\frac{x}{2L}}$ is the Williamson parameter, $\mathrm{Pr} = \frac{\mu_\infty c_p}{\kappa_\infty}$ is the Prandtl number, $\gamma = \frac{\nu_\infty L}{k_0 U_0}e^{\frac{-x}{L}}$ is the porous parameter, $\mathrm{Nb} = \frac{\tau D_B(C_w - C_\infty)}{\nu_\infty}$ is the Brownian motion parameter, $\mathrm{Gr}_C = \frac{2Lg\beta_C(C_w-C_\infty)}{U_0 e^{\frac{2x}{L}}}$ is the local modified Grashof number, $\mathrm{Gr}_T = \frac{2Lg\beta_T(T_w-T_\infty)}{U_0 e^{\frac{2x}{L}}}$ is the local Grashof number, $\mathrm{Sc} = \frac{\nu_\infty}{D_B}$ is the Schmidt number, $\mathrm{Ec} = \frac{U_w^2}{(T_w-T_\infty)c_p}$ is the Eckert number, and $\mathrm{Nt} = \frac{\tau D_T(T_w-T_\infty)}{\nu_\infty T_\infty}$ is the thermophoresis parameter. Accordingly, the Sherwood number, Nusselt number, and skin friction are [27]:

$$\begin{aligned}
&\sqrt{2}\mathrm{Cf}_x\,\mathrm{Re}_x^{1/2} = -\left(f''(0) + \frac{W_e}{2}f''^2(0)\right)e^{-\alpha\theta(0)},\\
&\frac{1}{\sqrt{2}}\mathrm{Re}_x^{-1/2}\,e^{\frac{-x}{2L}}\,\mathrm{Nu}_x = -\theta'(0),\\
&\frac{1}{\sqrt{2}}\mathrm{Re}_x^{-1/2}\,e^{\frac{-x}{2L}}\,\mathrm{Sh}_x = -\phi'(0),
\end{aligned}$$

where $\mathrm{Re}_x = \frac{U_w L}{\nu_\infty}$ is the local Reynolds number.

3 Solution procedure

3.1 Basic concepts about Appell–Changhee polynomials

It is well-known that Changhee polynomials $\mathrm{Ch}_m(t)$ are usually defined using generating functions (see [19, 22]),

$$\frac{2}{z+2}(1-z)^t = \sum_{m=0}^{\infty}\mathrm{Ch}_m(t)\frac{z^m}{m!},$$

where $\mathrm{Ch}_m = \mathrm{Ch}_m(0)$ are the Changhee numbers, see [19]. These polynomials can also be given in the following form:

$$\mathrm{Ch}_m(t) = \sum_{m=0}^{\infty}S_1(m,\ell)E_\ell(t),$$

where $S_1(m,\ell)$ and $E_\ell(t)$ are Sterling numbers of the first kind and Euler polynomials, respectively. However, the Appell-type Changhee polynomials $\mathrm{Ch}_m^*(t)$ are defined by the generating function given by [28]

$$\frac{2}{z+2}e^{tz} = \sum_{m=0}^{\infty}\mathrm{Ch}_m^*(t)\frac{z^m}{m!}.$$

The ACPs of degree m are defined by

$$\mathrm{Ch}_m^*(t) = \sum_{j=0}^{m}\binom{m}{j}\mathrm{Ch}_{m-j}^*t^j. \tag{14}$$

From formula (14), one can easily get that

$$\frac{d}{dt}\mathrm{Ch}_m^*(t) = m\mathrm{Ch}_{m-1}^*(t), \tag{15}$$

therefore from (15), we can confirm the following formula:

$$\mathrm{Ch}_m^*(t) = \int_0^t m\mathrm{Ch}_{m-1}^*(y)\,dy + \mathrm{Ch}_m^*.$$

It is also worth noting that $\mathrm{Ch}_0^* = 1$ and $2\mathrm{Ch}_m^* + m\mathrm{Ch}_{m-1}^* = 0$, $\forall m \geq 1$.

In addition, we can prove that the ACPs satisfy the following identity:

$$\int_0^1 \mathrm{Ch}_n^*(t)\mathrm{Ch}_m^*(t)\,dt = \sum_{i=0}^{m}\sum_{k=0}^{m-i}\binom{m}{i}\frac{(-1)^{m-i-1}(m-i)\binom{m-i}{k}\mathrm{Ch}_k^*(1)\mathrm{Ch}_i^*}{(2(m-i)-k+1)\binom{2(m-i)-k}{m-i}}. \tag{16}$$

Let $\{\mathrm{Ch}_i^*(t)\}_{i=1}^m \subset \mathrm{L}^2[0,1]$ be the set of ACPs and suppose that

$$\Omega = \mathrm{Span}\{\mathrm{Ch}_i^*(t)\}_{i=1}^m,$$

is a finite-dimensional subspace of $L^2[0,1]$ [28].

For a function $g(t)$ of $L^2[0,1]$, one has a good and unique approximation of it in Ω. If $g^*(t)$ is the unique approximation of $g(t)$, we can write the following error estimate:

$$\|g(t)-g^*(t)\|_2 \le \|g(t)-h(t)\|_2, \quad \forall h(t)\in\Omega.$$

But because Ω is a closed subspace of $L^2[0,1]$, according to [29], we can write $L^2[0,1]=\Omega\oplus\mathbf{\Omega}^\perp$, where $\mathbf{\Omega}^\perp$ denotes the orthogonal complement of Ω, and so we have $g(t)=h(t)+r(t)$ and then $r(t)=g(t)-h(t)$, which also means that $g(t)-g^*(t)\in\Omega^\perp$. Therefore, this confirms the following:

$$\langle g(t)-g^*(t), h(t)\rangle = 0, \quad \forall h(t)\in\Omega, \tag{17}$$

where $\langle\cdot,\cdot\rangle$ denotes the inner product.

Since $g^*(t)\in\Omega$, we can write the following:

$$g(t)\approx g^*(t)=\sum_{i=0}^{N} c_i\mathrm{Ch}_i^*(t)=\mathbf{C}^T\mathbf{Ch}^*(t), \tag{18}$$

where

$$\mathbf{C}=[c_1,c_2,\dots,c_N]^T, \qquad \mathbf{Ch}^*(t)=[\mathrm{Ch}_1^*(t),\mathrm{Ch}_2^*(t),\dots,\mathrm{Ch}_N^*(t)]^T.$$

By taking $h(t)=\mathrm{Ch}_i^*(t)$ and substituting equation (18) into (17), we get

$$\langle g(t)-\mathbf{C}^T\mathbf{Ch}^*(t), \mathrm{Ch}_i^*(t)\rangle = 0.$$

Also from (18), we can see that

$$\langle g(t), \mathbf{Ch}^*(t)\rangle = \mathbf{C}^T\langle\mathbf{Ch}^*(t),\mathbf{Ch}^*(t)\rangle = \mathbf{C}^T\mathbb{A}, \tag{19}$$

where $\mathbb{A}=\langle\mathbf{Ch}^*(t),\mathbf{Ch}^*(t)\rangle$ is an $N\times N$ matrix, defined by

$$\mathbb{A}=\langle\mathbf{Ch}^*(t),\mathbf{Ch}^*(t)\rangle=\int_0^t \mathbf{Ch}^*(\tau)\mathbf{Ch}^{*T}(\tau)\,d\tau,$$

and $\mathbb{A}$ can be computed by using (16). Therefore, the coefficients' vector from (19) can take the form

$$\mathbf{C}=\mathbb{A}^{-1}\langle g(t),\mathbf{Ch}^*(t)\rangle.$$

In this subsection, we will show that the nth derivative D^n of the function $g^*(\eta)$ given in (18) can be approximated through the following theorem.

Theorem 1 *The derivative of order $n > 0$ for the function $g^*(\eta)$ given in (18) can be approximated by*

$$D^n g^*(\eta) = \sum_{i=n}^{N} \sum_{j=n}^{i} c_i \chi_{i,j,n} \eta^{j-n}, \tag{20}$$

where Ch^*_{i-j} is the Changhee number, and $\chi_{i,j,n}$ is given by

$$\chi_{i,j,n} = \frac{(i)!\mathrm{Ch}^*_{i-j}}{(i-j)!(j-n)!}.$$

Proof Considering the ACP, $\mathrm{Ch}^*_i(\eta)$ of degree i, with $i = 0, 1, \ldots, N$, and by using (18), we can get

$$\begin{aligned} D^n g^*(\eta) &= \sum_{i=0}^{N} c_i D^n \mathrm{Ch}^*_i(\eta) = \sum_{i=n}^{N} \sum_{j=n}^{i} c_i \frac{(i!)\mathrm{Ch}^*_{i-j}}{(j!)(i-j)!} D^n \eta^j \\ &= \sum_{i=n}^{N} \sum_{j=n}^{i} c_i \frac{(i!)\mathrm{Ch}^*_{i-j}}{(i-j)!(j-n)!} \eta^{j-n} = \sum_{i=n}^{N} \sum_{j=n}^{i} c_i \chi_{i,j,n} \eta^{j-n}, \end{aligned}$$

where $\chi_{i,j,n}$ is given in (20), and this completes the proof. □

3.2 Solution procedure using SCM

We will implement the SCM to solve the system (9)–(13) numerically. We approximate $f(\eta)$, $\theta(\eta)$, and $\phi(\eta)$ by $f_N(\eta)$, $\theta_N(\eta)$, and $\phi_N(\eta)$, respectively, as follows:

$$f_N(\eta) = \sum_{i=0}^{N} a_i \mathrm{Ch}^*_i(\eta), \qquad \theta_N(\eta) = \sum_{i=0}^{N} b_i \mathrm{Ch}^*_i(\eta), \qquad \phi_N(\eta) = \sum_{i=0}^{N} c_i \mathrm{Ch}^*_i(\eta). \tag{21}$$

By substituting (20) and (21) into the system (9)–(11), we get

$$\begin{aligned} &\left(1 + W_e \sum_{i=2}^{N} \sum_{j=2}^{i} a_i \chi_{i,j,2} \eta^{j-2}\right)\left(\sum_{i=3}^{N} \sum_{j=3}^{i} a_i \chi_{i,j,3} \eta^{j-3}\right) - \alpha \left(\sum_{i=1}^{N} \sum_{j=1}^{i} b_i \chi_{i,j,1} \eta^{j-1}\right) \\ &\quad \times \left(\sum_{i=2}^{N} \sum_{j=2}^{i} a_i \chi_{i,j,2} \eta^{j-2}\right)\left(1 + \frac{W_e}{2}\left(\sum_{i=2}^{N} \sum_{j=2}^{i} a_i \chi_{i,j,2} \eta^{j-2}\right)\right) \\ &\quad - \gamma \left(\sum_{i=1}^{N} \sum_{j=1}^{i} a_i \chi_{i,j,1} \eta^{j-1}\right) + \exp\left[\alpha \left(\sum_{i=0}^{N} b_i \mathrm{Ch}^*_i(\eta)\right)\right] \\ &\quad \times \left(\left(\sum_{i=0}^{N} a_i \mathrm{Ch}^*_i(\eta)\right)\left(\sum_{i=2}^{N} \sum_{j=2}^{i} a_i \chi_{i,j,2} \eta^{j-2}\right)\right. \\ &\quad - 2\left(\sum_{i=1}^{N} \sum_{j=1}^{i} a_i \chi_{i,j,1} \eta^{j-1}\right)^2 - M \left(\sum_{i=1}^{N} \sum_{j=1}^{i} a_i \chi_{i,j,1} \eta^{j-1}\right) \end{aligned} \tag{22}$$

$$+\left(\sum_{i=0}^{N}(\mathrm{Gr}_T b_i+\mathrm{Gr}_C c_i)\mathrm{Ch}_i^*(\eta)\right)\Bigg)=0,$$

$$\begin{aligned}
&\frac{1}{\mathrm{Pr}}\left(\left(1+\varepsilon\left(\sum_{i=0}^{N}b_i\mathrm{Ch}_i^*(\eta)\right)\right)\left(\sum_{i=2}^{N}\sum_{j=2}^{i}b_i\chi_{i,j,2}\eta^{j-2}\right)+\varepsilon\left(\sum_{i=1}^{N}\sum_{j=1}^{i}b_i\chi_{i,j,1}\eta^{j-1}\right)^2\right)\\
&\quad+\left(\sum_{i=0}^{N}a_i\mathrm{Ch}_i^*(\eta)\right)\left(\sum_{i=1}^{N}\sum_{j=1}^{i}b_i\chi_{i,j,1}\eta^{j-1}\right)-\left(\sum_{i=0}^{N}b_i\mathrm{Ch}_i^*(\eta)\right)\\
&\quad\times\left(\sum_{i=1}^{N}\sum_{j=1}^{i}a_i\chi_{i,j,1}\eta^{j-1}\right)+\mathrm{Nt}\left(\sum_{i=1}^{N}\sum_{j=1}^{i}b_i\chi_{i,j,1}\eta^{j-1}\right)^2\\
&\quad+\mathrm{Nb}\left(\sum_{i=1}^{N}\sum_{j=1}^{i}b_i\chi_{i,j,1}\eta^{j-1}\right)\left(\sum_{i=1}^{N}\sum_{j=1}^{i}c_i\chi_{i,j,1}\eta^{j-1}\right)\\
&\quad+M\mathrm{Ec}\left(\sum_{i=1}^{N}\sum_{j=1}^{i}a_i\chi_{i,j,1}\eta^{j-1}\right)^2+\mathrm{Ec}\left(\left(\sum_{i=2}^{N}\sum_{j=2}^{i}a_i\chi_{i,j,2}\eta^{j-2}\right)^2\right.\\
&\quad\left.+\frac{W_e}{2}\left(\sum_{i=2}^{N}\sum_{j=2}^{i}a_i\chi_{i,j,2}\eta^{j-2}\right)^3\right)\exp\left[-\alpha\left(\sum_{i=0}^{N}b_i\mathrm{Ch}_i^*(\eta)\right)\right]\\
&\quad+\frac{1}{\mathrm{Pr}}\left(1+\varepsilon\left(\sum_{i=0}^{N}b_i\mathrm{Ch}_i^*(\eta)\right)\right)\left(D_1\left(\sum_{i=1}^{N}\sum_{j=1}^{i}a_i\chi_{i,j,1}\eta^{j-1}\right)\right.\\
&\quad\left.+E_1\left(\sum_{i=0}^{N}b_i\mathrm{Ch}_i^*(\eta)\right)\right)=0,
\end{aligned}\tag{23}$$

$$\begin{aligned}
&\left(\sum_{i=2}^{N}\sum_{j=2}^{i}c_i\chi_{i,j,2}\eta^{j-2}\right)+\mathrm{Sc}\left(\sum_{i=0}^{N}a_i\mathrm{Ch}_i^*(\eta)\right)\left(\sum_{i=1}^{N}\sum_{j=1}^{i}c_i\chi_{i,j,1}\eta^{j-1}\right)\\
&\quad+\frac{\mathrm{Nt}}{\mathrm{Nb}}\left(\sum_{i=2}^{N}\sum_{j=2}^{i}b_i\chi_{i,j,2}\eta^{j-2}\right)=0.
\end{aligned}\tag{24}$$

By collocation of the previous equations (22)–(24) at $N-1$ points $\eta_r=\frac{r}{N-1}+1$, $i=1,2,\dots,N-1$, they will reduce to a system of algebraic equations in the coefficients a_i, b_i, c_i, $i=0,1,2,\dots,N$.

In addition, the boundary conditions (12)–(13) can be expressed by substituting Eq. (21) into (12)–(13) to find the following equations:

$$\begin{aligned}
&\sum_{i=0}^{N}\mathrm{Ch}_i^*a_i=S,\qquad \sum_{i=0}^{N}\mathrm{Ch}_i^*b_i=1,\qquad \sum_{i=0}^{N}\mathrm{Ch}_i^*c_i=1,\\
&\sum_{i=0}^{N}a_iH1_i=1+\lambda\left(\left(\sum_{i=0}^{N}a_iH2_i\right)+\frac{W_e}{2}\left(\sum_{i=0}^{N}a_iH2_i\right)^2\right)\exp\left[-\alpha\left(\sum_{i=0}^{N}b_i\mathrm{Ch}_i^*\right)\right],
\end{aligned}\tag{25}$$

$$\sum_{i=0}^{N}a_i\mathrm{Ch}_i^{*\prime}(\eta_\infty)=0,\qquad \sum_{i=0}^{N}b_i\mathrm{Ch}_i^*(\eta_\infty)=0,\qquad \sum_{i=0}^{N}c_i\mathrm{Ch}_i^*(\eta_\infty)=0,\tag{26}$$

where $H1_i = \mathrm{Ch}_i^{*\prime}(0)$, $H2_i = \mathrm{Ch}_i^{*\prime\prime}(0)$, and the values of Ch_i^*, $i = 0, 1, 2, \dots, N$ can be computed by using the iterative formula

$$2\mathrm{Ch}_i^* + i\mathrm{Ch}_{i-1}^* = 0, \quad \forall i \geq 1.$$

Equations (25)–(26), together with equations (22)–(24), give a system of $3(N + 1)$ algebraic equations. We will solve this system for the unknowns a_i, b_i, c_i, $i = 0, 1, \dots, N$, by using the Newton iteration method. This, in turn, will leads us to compute the approximate solution by substitution in the form (21).

4 Code validation

In this section, we compare the numerical values of the skin friction coefficient against various values of the Williamson parameter W_e with the data calculated by Nadeem and Hussain [30] to confirm our numerical results that were achieved using the spectral collocation method, which depends on the characteristics of the ACPs. As shown in Table 1, these findings are closely linked to those reported in the literature by Nadeem and Hussain [30]. Therefore, we can confidently state that the data presented here is accurate.

5 Results and discussion

The findings of using the SCM to establish the significant features of the flow, heat, and mass transfer characteristics with nanoparticles are shown in Figs. 2 through 13 and in Table 2. Figure 2 depicts how a magnetic parameter M affects temperature $\theta(\eta)$, velocity $f'(\eta)$, and concentration $\phi(\eta)$ graphs, respectively. It can be shown in Fig. 2 that the Lorentz force becomes strong for large magnetic field parameters, increasing the fluid resistance and causing velocity to decrease. Additionally, it is observed that as the magnetic parameter increases, species concentration drops, followed by a decrease in the thickness

Table 1 Values of skin friction $\sqrt{2}\mathrm{Cf}_x \mathrm{Re}_x^{1/2}$ with various W_e and the results of Nadeem and Hussain [30] when $\gamma = \mathrm{Gr}_T = \mathrm{Gr}_C = M = \alpha = \lambda = 0$ and $S = 0.2$

W_e	Nadeem and Hussain [30]	Present work
0.0	1.19298	1.1929799857
0.1	1.16468	1.1646900153
0.2	1.13365	1.1336499198
0.3	1.09881	1.0988099850

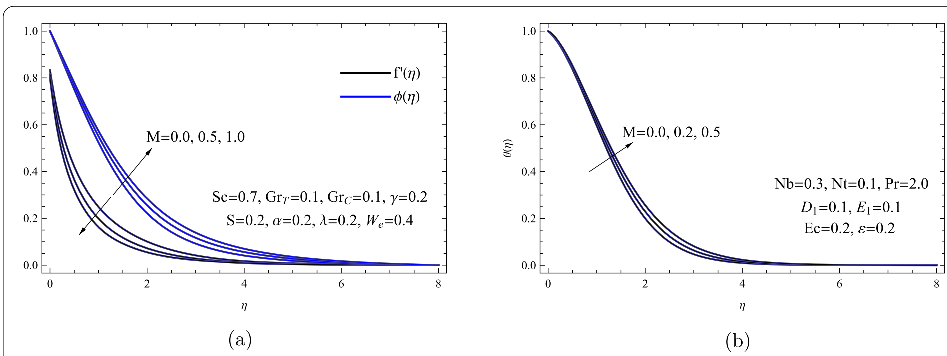

Figure 2 (a) $f'(\eta)$ and $\phi(\eta)$ for various M; (b) $\theta(\eta)$ for various M

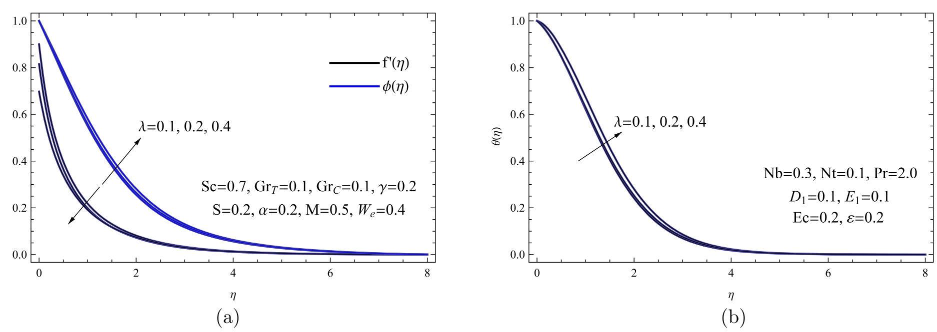

Figure 3 (a) $f'(\eta)$ and $\phi(\eta)$ for various λ; (b) $\theta(\eta)$ for various λ

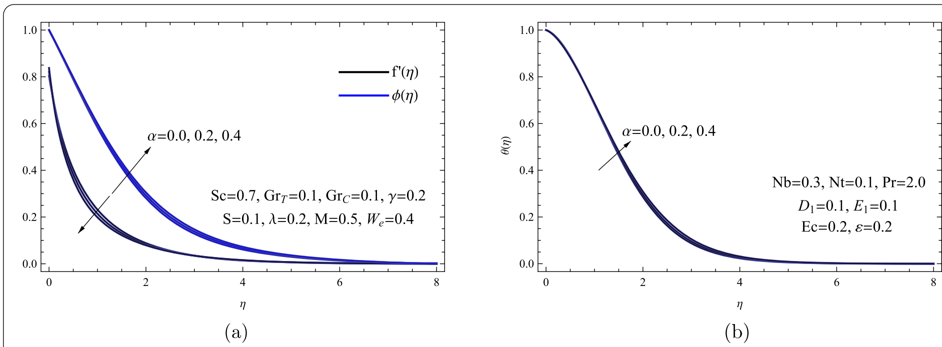

Figure 4 (a) $f'(\eta)$ and $\phi(\eta)$ for various α; (b) $\theta(\eta)$ for various α

of the solutal boundary layer. Furthermore, it appears that a rise in the magnetic parameter improves the temperature distribution.

Figure 3 displays the variations in the fields of velocity $f'(\eta)$, temperature $\theta(\eta)$, and concentration $\phi(\eta)$ for various values of the slip velocity parameter λ. Diminishing behavior is observed in the velocity field with rising values of the slip velocity parameter λ, whereas the temperature field exhibits the opposite trend for the same parameter. It is shown that increasing the slip velocity parameter decreases the volume friction of nanoparticles, improving the boundary layer thickness and concentration profile. Physically, the reduction in nanofluid velocity associated with the slip velocity parameter can be explained by slip flow, which refers to the situation where the fluid near a solid surface moves at a different speed compared to the surface itself. When nanoparticles are present in nanofluids near the solid surface, they form a boundary layer that influences the flow behavior of the fluid. The slip velocity parameter quantifies slip flow and represents the relative velocity between the fluid and the solid surface.

For a particular viscosity parameter α values that define the flow behavior and the heat mass transfer spread through the boundary layer, Fig. 4 illustrates the velocity, temperature, and concentration curves. It was made clear that an increase in the viscosity parameter led to a greater improvement in the panoplied's viscosity, which was related to the fact that when the viscosity parameter increases, the fluid velocity decreases. Additionally, a bigger viscosity parameter leads to stronger mass and heat transport, which enhances the temperature and concentration fields. Physically, the viscosity parameter gauges a fluid's ability to flow. Nanoparticles alter the viscosity of nanofluids when they are added. As a

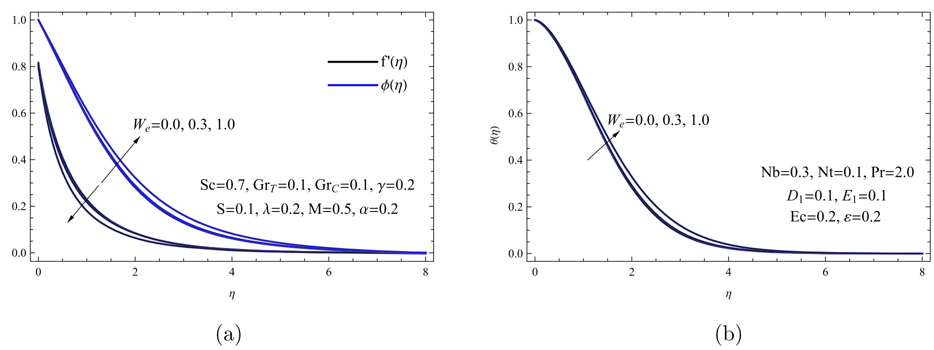

Figure 5 (a) $f'(\eta)$ and $\phi(\eta)$ for various W_e; (b) $\theta(\eta)$ for various W_e

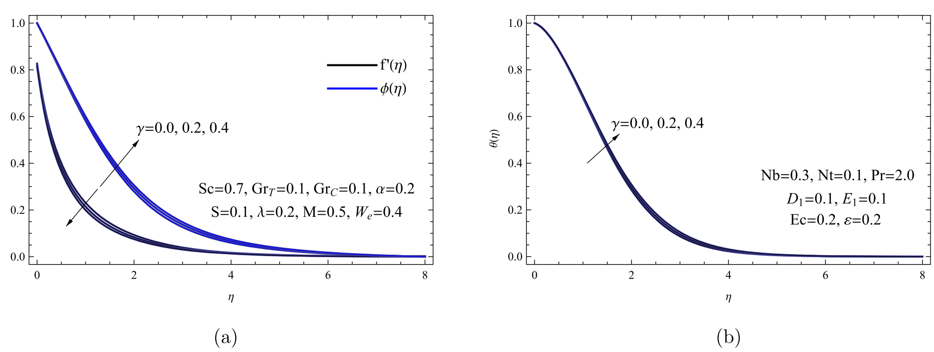

Figure 6 (a) $f'(\eta)$ and $\phi(\eta)$ for various γ; (b) $\theta(\eta)$ for various γ

result, the velocity of the nanofluid decreases. The addition of nanoparticles alters the interactions between the fluid molecules, increasing the viscosity of the nanofluid as a whole. This increased viscosity causes the fluid to experience greater internal friction, which slows the flow and lowers the velocity.

Figure 5 examines the impact of the Williamson parameter W_e on the distributions of $f'(\eta)$, $\theta(\eta)$, and $\phi(\eta)$. In contrast to concentration and temperature distribution, the velocity distribution changes. The temperature and concentration distribution advance as the Williamson parameter increases. It indicates that as nanoparticle mobility increases, the thermal conductivity of nanofluids also increases, which boosts the heat- and mass-transfer mechanisms.

The velocity, concentration, and temperature profiles for several porous parameter γ values are shown in Fig. 6. In this case, raising the porous parameter γ induces the velocity profile to drastically deteriorate, although the temperature and concentration fields exhibit the opposite tendency. Additionally, the porous parameter produces a small improvement in the thickness of the thermal boundary layer.

Figure 7 shows how raising the local Grashof number Gr_T improves the velocity profile $f'(\eta)$. Physical justification can be found in the fact that as the local Grashof number increases, the convection mechanism improves, increasing the nanofluid velocity. In contrast, the temperature $\theta(\eta)$ and concentration $\phi(\eta)$ fields exhibit different behavior. Physically, the Grashof number is a dimensionless parameter that captures the equilibrium between buoyant and viscous forces in fluid flow. The following physical explanation ex-

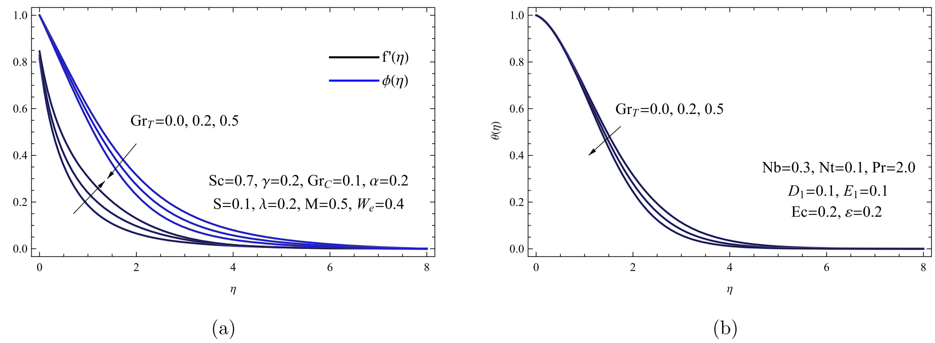

Figure 7 (a) $f'(\eta)$ and $\phi(\eta)$ for various Gr_T; (b) $\theta(\eta)$ for various Gr_T

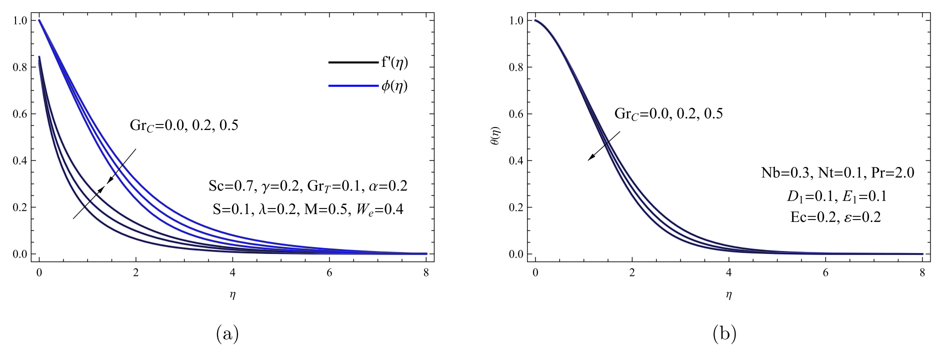

Figure 8 (a) $f'(\eta)$ and $\phi(\eta)$ for various Gr_C; (b) $\theta(\eta)$ for various Gr_C

plains why a higher Grashof number could result in a faster nanofluid: An increase in the Grashof number denotes a greater dominance of buoyant forces over viscous forces. The fluid consequently encounters a stronger pushing force as a result of temperature or density variations. This more powerful pushing force causes the nanofluid to move more quickly, which improves convective heat transfer. As a result, an increase in the Grashof number causes the nanofluid velocity to increase, encouraging more active fluid flow and better convective heat transfer.

Plotted in Figs. 8(a) and 8(b) are the findings of the velocity, temperature, and concentration distributions for the local modified Grashof number Gr_C operating in the laminar Williamson nanofluid flow zone. According to the findings in these graphs, the velocity field and boundary layer thickness both improve as the locally modified Grashof number increases. Additionally, the opposite is shown for the same parameter on mass and heat transport.

The relationship between the thermal conductivity parameter ε and the Williamson nanofluid flow and heat mass properties is depicted in Fig. 9. This graph demonstrates that the velocity $f'(\eta)$, concentration $\phi(\eta)$, and temperature $\theta(\eta)$ profiles through the boundary layer region are ascending in nature for larger values of the thermal conductivity parameter. This is because the conductivity behavior of the nanofluid advances as the thermal conductivity parameter increases. Physically, when it comes to nanofluids, the presence of nanoparticles can increase the fluid's thermal conductivity parameter, which is a measure of a material's capacity to conduct heat. And so, the nanofluid exhibits higher tempera-

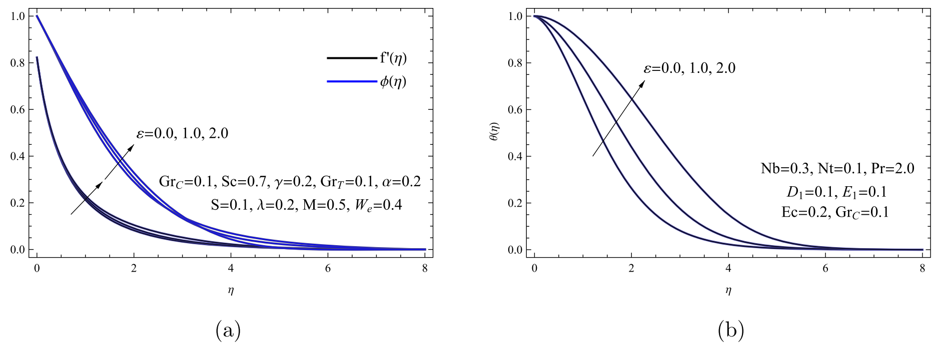

Figure 9 (a) $f'(\eta)$ and $\phi(\eta)$ for various ε; (b) $\theta(\eta)$ for various ε

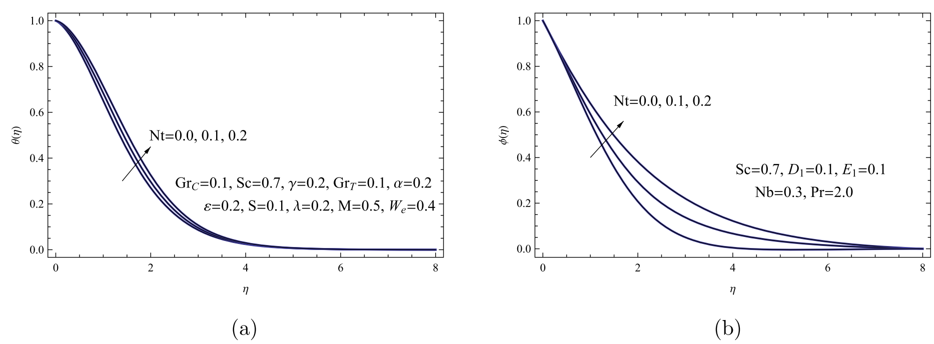

Figure 10 (a) $\theta(\eta)$ for various Nt; (b) $\phi(\eta)$ for various Nt

tures as a result of this increased thermal conductivity parameter, which is brought on by the fluid's improved capacity to conduct and dissipate heat.

For various values of the thermophoresis parameter Nt, Fig. 10 depicts the variations in the concentration and temperature fields. It has been noted that as the thermophoresis parameter is elevated, both concentration and temperature profiles rise because thermophoresis is a phenomenon by which small particles are drawn from hot to cool surfaces, which causes the temperature to rise.

Figure 11 shows how the temperature $\theta(\eta)$ and concentration $\phi(\eta)$ fields for nanofluids are affected by the Brownian motion parameter Nb. This figure illustrates how raising the Brownian motion parameter causes fluid particles to move randomly, which raises the concentration and temperature profiles.

The temperature profile $\theta(\eta)$ within the thermal boundary layer region is affected by Eckert number Ec, as shown in Fig. 12(a), since an increase in the Eckert number speeds up the movement of kinetic energy. Fluid particles collide more regularly as a consequence, which causes kinetic energy to be converted into heat energy in the process. As a result, the temperature profile rises, as seen in the graph. Figure 12(b) shows how the space-dependent heat source parameter D_1 influences the temperature profile. The fluid temperature increases for high values of the space-dependent heat source parameter; this phenomenon is physically maintained because high values of D_1 result in increased heat generation and increased temperature distribution for a nanofluid.

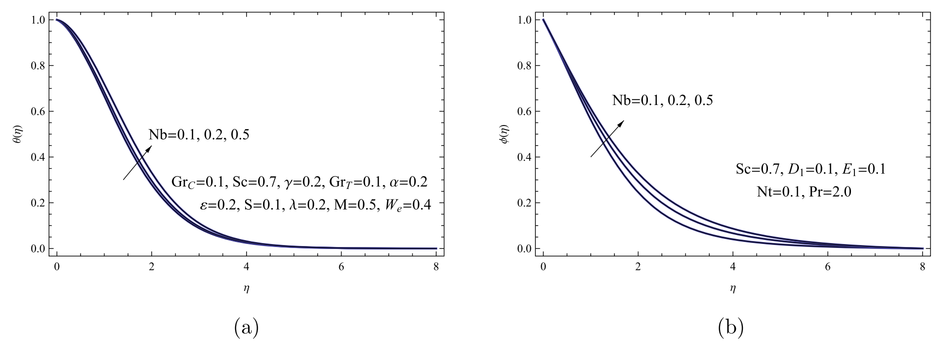

Figure 11 (a) $\theta(\eta)$ for various Nb; (b) $\phi(\eta)$ for various Nb

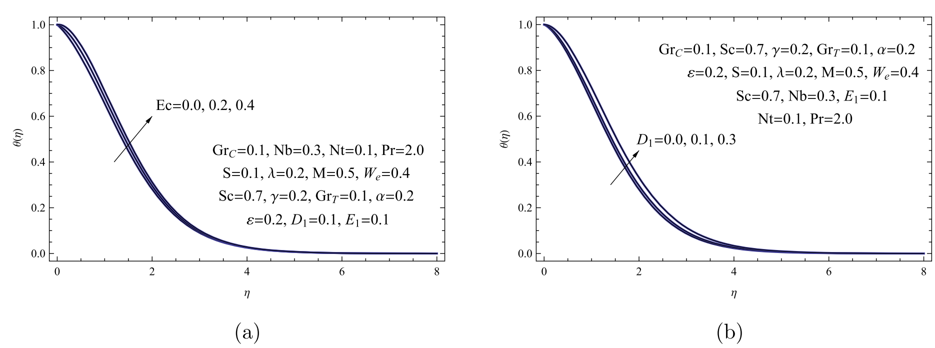

Figure 12 (a) $\theta(\eta)$ for various Ec; (b) $\theta(\eta)$ for various D_1

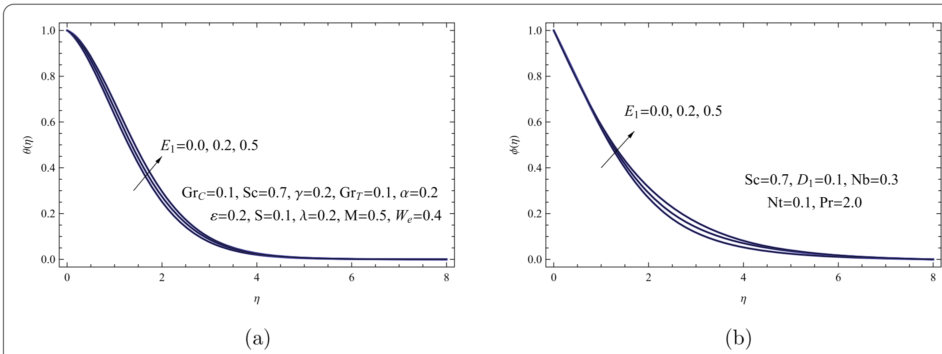

Figure 13 (a) $\theta(\eta)$ for various E_1; (b) $\phi(\eta)$ for various E_1

The effect of the temperature-dependent heat source parameter E_1 on the temperature and concentration profile is seen in Fig. 13. The graph demonstrates how increasing the temperature-dependent heat source parameter increased the capacity of heat and mass transference, leading to an increase in both the nanofluid temperature and concentration.

Table 2 shows the variations in the skin friction coefficient $\sqrt{2}\mathrm{Cf}_x \mathrm{Re}_x^{1/2}$, Nusselt number $\frac{1}{\sqrt{2}} \mathrm{Re}_x^{-1/2} e^{\frac{-x}{2L}} \mathrm{Nu}_x$, and Sherwood number $\frac{1}{\sqrt{2}} \mathrm{Re}_x^{-1/2} e^{\frac{-x}{2L}} \mathrm{Sh}_x$ caused by modifying the magnetic field parameter, slip velocity parameter, local Grashof number, thermal conductivity parameter, thermophoresis parameter, porous parameter, local modified Grashof number, and Williamson parameter. It is evident that with high values of the thermal conductivity,

Table 2 Values of $\sqrt{2}\mathrm{Cf}_x\,\mathrm{Re}_x^{1/2}$, $\frac{1}{\sqrt{2}}\,\mathrm{Re}_x^{-1/2}\,e^{\frac{-x}{2L}}\,\mathbf{Nu}_x$, and $\frac{1}{\sqrt{2}}\,\mathrm{Re}_x^{-1/2}\,e^{\frac{-x}{2L}}\,\mathbf{Sh}_x$ for different values of M, W_e, λ, M, α, Gr_T, γ, Gr_C, ε, and Nt with $\mathrm{Nb} = 0.3$, $\mathrm{Pr} = 2.0$, $\mathrm{Sc} = 0.7$, $E_1 = D_1 = 0.1$

M	λ	α	W_e	γ	Gr_T	Gr_C	ε	Nt	$\sqrt{2}\mathrm{Cf}_x\,\mathrm{Re}_x^{1/2}$	$-\theta'(0)$	$-\phi'(0)$
0.0	0.2	0.2	0.4	0.2	0.1	0.1	0.2	0.1	0.833653	0.170981	0.490641
0.5	0.2	0.2	0.4	0.2	0.1	0.1	0.2	0.1	0.894223	0.072283	0.393338
1.0	0.2	0.2	0.4	0.2	0.1	0.1	0.2	0.1	0.997098	0.060109	0.322310
0.5	0.1	0.2	0.4	0.2	0.1	0.1	0.2	0.1	0.997533	0.052086	0.399021
0.5	0.2	0.2	0.4	0.2	0.1	0.1	0.2	0.1	0.894223	0.072283	0.393338
0.5	0.4	0.2	0.4	0.2	0.1	0.1	0.2	0.1	0.832701	0.113745	0.374296
0.5	0.2	0.0	0.4	0.2	0.1	0.1	0.2	0.1	0.978704	0.068678	0.401294
0.5	0.2	0.2	0.4	0.2	0.1	0.1	0.2	0.1	0.894223	0.072283	0.393338
0.5	0.2	0.4	0.4	0.2	0.1	0.1	0.2	0.1	0.811372	0.125345	0.384812
0.5	0.2	0.2	0.0	0.2	0.1	0.1	0.2	0.1	0.972188	0.072382	0.403296
0.5	0.2	0.2	0.3	0.2	0.1	0.1	0.2	0.1	0.919105	0.068511	0.396582
0.5	0.2	0.2	1.0	0.2	0.1	0.1	0.2	0.1	1.001452	0.038467	0.364299
0.5	0.2	0.2	0.4	0.0	0.1	0.1	0.2	0.1	0.865521	0.075244	0.404453
0.5	0.2	0.2	0.4	0.2	0.1	0.1	0.2	0.1	0.894223	0.072283	0.393338
0.5	0.2	0.2	0.4	0.4	0.1	0.1	0.2	0.1	0.937923	0.068783	0.383043
0.5	0.2	0.2	0.4	0.2	0.0	0.1	0.2	0.1	0.926203	0.066614	0.375611
0.5	0.2	0.2	0.4	0.2	0.2	0.1	0.2	0.1	0.862694	0.076390	0.408515
0.5	0.2	0.2	0.4	0.2	0.5	0.1	0.2	0.1	0.769952	0.083254	0.445226
0.5	0.2	0.2	0.4	0.2	0.1	0.0	0.2	0.1	0.924370	0.067664	0.376091
0.5	0.2	0.2	0.4	0.2	0.1	0.2	0.2	0.1	0.864871	0.075555	0.407749
0.5	0.2	0.2	0.4	0.2	0.1	0.5	0.2	0.1	0.780159	0.081454	0.441202
0.5	0.2	0.2	0.4	0.2	0.1	0.1	0.0	0.1	0.895334	0.070789	0.391162
0.5	0.2	0.2	0.4	0.2	0.1	0.1	1.0	0.1	0.890185	0.048911	0.394952
0.5	0.2	0.2	0.4	0.2	0.1	0.1	2.0	0.1	0.884849	0.010936	0.398894
0.5	0.2	0.2	0.4	0.2	0.1	0.1	0.2	0.0	0.894151	0.102421	0.400172
0.5	0.2	0.2	0.4	0.2	0.1	0.1	0.2	0.1	0.894223	0.072283	0.393338
0.5	0.2	0.2	0.4	0.2	0.1	0.1	0.2	0.2	0.895166	0.045356	0.377218

Williamson, porous, thermophoresis, local Grashof, and magnetic parameters, the local Nusselt number declines. The local Sherwood number is shown in the same table to have a diminishing function for the slip velocity, magnetic field, viscosity, and porous parameters. It's vital to remember that when the slip velocity, viscosity parameter, and thermal conductivity parameter values rise, the local skin-friction coefficient drops. However, this impact is inverted for the high values of the magnetic, porous, and Williamson parameters.

6 Conclusions

In this work, non-Newtonian Williamson nanofluid flow characteristics caused by a vertical exponential stretching sheet were addressed. The spectral collocation technique which basically depends on the properties of the Appell-type Changhee polynomials was used to give a numerical solution to the aforementioned problem. The flow was thought to be in a steady state. Williamson nanofluid flows' slip velocity phenomena, the influence of magnetic fields, heat generation, and viscous dissipation all play a role in how this study is observed. Graphical analysis was used to view and analyze the impact of the embedded factors. These numerical calculations and mathematical modeling have essential applications, particularly in cooling operations. As a consequence, the present study can specify several essential aspects that are crucial in engineering applications. The key findings are as follows:

1. The skin friction decreases as the parameters for viscosity, slip velocity, and the local Grashof number are improved.
2. In contrast to the effects of the magnetic field, slip velocity, and viscosity parameters on fluid motion, an increase in the local Grashof number causes fluid velocity to accelerate.
3. The Nusselt number is increased by the slip velocity and local modified Grashof numbers, whereas it is decreased by the magnetic, Williamson, and porous parameters.
4. The temperature of nanofluids is controlled by the magnetic field and higher levels of the local Grashof number.
5. By increasing the values of the thermophoresis parameter, the Nusselt number declines, whereas the viscosity parameter exhibits the reverse tendency.
6. Increased values of the variable viscosity parameter, Grashof number, modified Grashof number, and thermal conductivity parameter result in a decrease in the skin friction coefficient.
7. In future endeavors, it would be advantageous to broaden the scope of analysis conducted in this study by examining the impact of different variables such as nanoparticle concentration, porosity, and the chemical reaction on the flow behavior of non-Newtonian Williamson nanofluids.

Acknowledgements
The authors extend their appreciation to the Deanship of Scientific Research, Imam Mohammad Ibn Saud Islamic University (IMSIU), Saudi Arabia, for funding this research work through Grant No. 221412018.

Funding
Not applicable.

Availability of data and materials
No data were used for this work.

Declarations

Ethics approval and consent to participate
Not applicable.

Competing interests
The authors declare no competing interests.

Author contributions
MMK and MMB wrote the main manuscript text and AMM prepared all figures. All authors reviewed the manuscript.

Received: 7 April 2023 Accepted: 9 July 2023 Published online: 10 August 2023

References
1. Williamson, R.V.: The flow of pseudo plastic materials. Ind. Eng. Chem. **21**, 1108–1111 (1929)
2. Dapra, I., Scarpi, G.: Perturbation solution for the pulsatile flow of a non-Newtonian Williamson fluid in a rock fracture. Int. J. Rock Mech. Min. Sci. **44**, 271–278 (2007)
3. Vasudev, C., Rao, U.R., Reddy, M.V., Rao, G.P.: Peristaltic pumping of Williamson fluid through a porous medium in a horizontal channel with heat transfer. Am. J. Sci. Ind. Res. **1**, 656–666 (2010)
4. Kothandapani, M., Prakash, J.: Effects of thermal radiation parameter and magnetic field on the peristaltic motion of Williamson nanofluids in a tapered asymmetric channel. Int. J. Heat Mass Transf. **81**, 234–245 (2015)
5. Hayat, T., Bashir, G., Waqas, M., Alsaedi, A.: MHD 2D flow of Williamson nanofluid over a nonlinear variable thicked surface with melting heat transfer. J. Mol. Liq. **223**, 836–844 (2016)
6. Nadeem, S., Hussain, S.T.: Analysis of MHD Williamson nano fluid flow over a heated surface. J. Appl. Fluid Mech. **9**, 729–739 (2016)
7. Megahed, A.M.: Williamson fluid flow due to a nonlinearly stretching sheet with viscous dissipation and thermal radiation. J. Egypt. Math. Soc. **27**, 12–19 (2019)
8. Megahed, A.M.: Steady flow of MHD Williamson fluid due to a continuously moving surface with viscous dissipation and slip velocity. Int. J. Mod. Phys. C **31**, 1–12 (2020)

9. Choi, U.S.: Enhancing thermal conductivity of fluids with nanoparticles. ASME FED **231**, 99–103 (1995)
10. Wang, X., Xu, X., Choi, S.: Thermal conductivity of nanoparticles–fluid mixture. J. Thermophys. Heat Transf. **13**, 474 (1999)
11. Keblinski, P., Phillpot, S.R., Choi, S., Eastman, J.A.: Mechanisms of heat flow in suspensions of nano-sized particles (nanofluids). Int. J. Heat Mass Transf. **45**, 855–863 (2002)
12. Zia, U., Muhammad, A., Saqib, Z., Yuming, C., Ilyas, K., Kottakkaran, S.N.: Computational analysis of the oscillatory mixed convection flow along a horizontal circular cylinder in thermally stratified medium. Comput. Mater. Continua **65**(1), 109–123 (2020)
13. Abbas, S.Z., Waqas, M., Thaljaoui, A., Zubair, M., Riahi, A., Chu, Y.M., Khan, W.A.: Modeling and analysis of unsteady second-grade nanofluid flow subject to mixed convection and thermal radiation. Soft Comput. **26**, 1033–1042 (2022)
14. Yu-Ming, C., Faisal, S., Ijaz, M.K., Seifedine, K., Zahra, A., Waqar, A.K.: Cattaneo–Christov double diffusions (CCDD) in entropy optimized magnetized second grade nanofluid with variable thermal conductivity and mass diffusivity. J. Mater. Res. Technol. **9**(6), 13977–13987 (2020)
15. Fazal, H., Seifedine, K., Yu-Ming, C., Mair, K., Ijaz, M.K.: Modeling and theoretical analysis of gyrotactic microorganisms in radiated nanomaterial Williamson fluid with activation energy. J. Mater. Res. Technol. **9**(5), 10468–10477 (2020)
16. Waqas, M., Ijaz, A.K., Zeeshan, A., Seifedine, K., Yu-Ming, C., Khan, W.A.: Interaction of heat generation in nonlinear mixed/forced convective flow of Williamson fluid flow subject to generalized Fourier's and Fick's concept. J. Mater. Res. Technol. **9**(5), 11080–11086 (2020)
17. Ijaz, M.K., Seifedine, K., Yu-Ming, C., Waqar, A.K., Amit, K.: Exploration of Lorentz force on a paraboloid stretched surface inflow of Ree–Eyring nanomaterial. J. Mater. Res. Technol. **9**(5), 10265–10275 (2020)
18. Muhammad, I., Tareq, S., Firooz, R.B., Shahab, N.S., Yu-Ming, C., Davood, T.: Two-phase analysis of heat transfer and entropy generation of water-based magnetite nanofluid flow in a circular microtube with twisted porous blocks under a uniform magnetic field. Powder Technol. **384**, 522–541 (2021)
19. Kim, D.S., Kim, T., Seo, J.J.: A note on Changhee polynomials and numbers. Adv. Stud. Theor. Phys. **7**(20), 993–1003 (2013)
20. Khader, M.M., Adel, M.: Numerical and theoretical treatment based on the compact finite difference and spectral collocation algorithms of the space fractional-order Fisher's equation. Int. J. Mod. Phys. C **31**(9), 1–15 (2020)
21. Adel, M., Assiri, T.A., Khader, M.M., Osman, M.S.: Numerical simulation by using the spectral collocation optimization method associated with Vieta–Lucas polynomials for a fractional model of non-Newtonian fluid. Results Phys. **41**, 1–8 (2022)
22. Lee, J.G., Jang, L.C., Seo, J.J., Choi, S.K., Kwon, H.I.: On Appell-type Changhee polynomials and numbers. Adv. Differ. Equ. **1**, 1–10 (2016)
23. Adel, M., Khader, M.M., Algelany, S.: High-dimensional chaotic Lorenz system: numerical treated using Changhee polynomials of the Appell type. Fractal Fract. **7**(398), 1–16 (2023)
24. Megahed, A.M.: Improvement of heat transfer mechanism through a Maxwell fluid flow over a stretching sheet embedded in a porous medium and convectively heated. Math. Comput. Simul. **187**, 97–109 (2021)
25. Mahmoud, M.A.A., Megahed, A.M.: Non-uniform heat generation effect on heat transfer of a non-Newtonian power-law fluid over a non-linearly stretching sheet. Meccanica **47**, 1131–1139 (2012)
26. Yi-Xia, L., Alshbool, M.H., Yu-Pei, L., Khan, I., Khan, M.R., Issakhov, A.: Heat and mass transfer in MHD Williamson nanofluid flow over an exponentially porous stretching surface. Case Stud. Therm. Eng. **26**, 100975 (2021)
27. Nadeem, S., Hussain, S.T., Lee, C.: Flow of a Williamson fluid over a stretching sheet. Braz. J. Chem. Eng. **30**, 619–625 (2013)
28. Kreyszig, E.: Introductory Functional Analysis with Applications, vol. 1. Wiley, New York (1978)
29. Saadatmandi, A., Dehghan, M.: A new operational matrix for solving fractional-order differential equations. Comput. Math. Appl. **59**(3), 1326–1336 (2010)
30. Nadeem, S., Hussain, S.T.: Heat transfer analysis of Williamson fluid over exponentially stretching surface. Appl. Math. Mech.-Engl. Ed. **35**, 489–502 (2014)

Publisher's Note